JOURNAL OF SPACECRAFT AND ROCKETS
Vol. 44, No. 5, September–October 2007

Experimentally Validated Model of a Membrane Strip with Multiple Actuators

Jamil M. Renno* and Daniel J. Inman†
Virginia Polytechnic Institute and State University, Blacksburg, Virginia 24061-0261

DOI: 10.2514/1.27843

This paper presents the modeling and experimental validation of a membrane strip actuated in bending and tension. This investigation is a prelude to the modeling of a circular membrane augmented with smart actuators around its outer rim. Two macrofiber composite bimorph actuators are attached near the ends of the membrane strip. We treat two configurations. In the first configuration, both bimorph actuators are excited in bending to change the shape of the membrane strip. In the second configuration, one bimorph acts in bending and the other bimorph acts in tension. The membrane strip is modeled as a nonuniform, nonhomogenous, Euler–Bernoulli beam under tension. The finite element method is used to facilitate the handling of the nonuniformities of the combined structure. Experimental results are used to validate the model developed. The prediction of the finite element model and the experimental results are in agreement.

Nomenclature

b	=	width of the membrane
b_k	=	width of the kth macrofiber composite wafer
c_D	=	internal damping coefficient of the membrane strip
c_k	=	internal damping coefficient of the kth macrofiber composite patch
d_{31}	=	electromechanical coupling coefficient of the macrofiber composite patch
E	=	Young's modulus of the membrane strip
E_k	=	Young's modulus of the wafer in the kth bimorph
EI	=	flexural rigidity of the structure
f_{ex}	=	natural frequency obtained experimentally
f_{FE}	=	natural frequency predicted by the finite element model
h	=	thickness of the membrane
h_k	=	thickness of the kth macrofiber composite patch
L	=	length of the membrane strip
L_k	=	length of the kth macrofiber composite patch
V_k	=	voltage input to the kth bimorph
γ	=	air damping coefficient
ρ_k	=	density of the kth macrofiber composite patch
ρ_m	=	density of the membrane
$\bar{\tau}$	=	nominal tension in the structure

I. Introduction

THE advent of the space age brought the need to study lightweight structures. The scientific community saw a significant example in 1958 in the field of spacecraft dynamics, when the Explorer satellite was launched. The vibration of the antennas resulted in energy transfer between the rigid and flexible motions of the satellite and led to nutational instabilities. This incident clearly brought attention to the need to model and study lightweight flexible structures.

Various government agencies, including the U.S. Air Force, the U.S. Department of Defense, NASA, and the Jet Propulsion Laboratory at the California Institute of Technology, have a mounting interest in the development and operation of lightweight space-based antennas and optical telescopes. Moreover, the U.S. Air Force Research Laboratory (AFRL) began a program of research on membrane technologies in 1997. Research performed at the AFRL clearly demonstrated that membrane mirrors are capable of producing high-quality images [1]. However, membrane mirrors are subject to various disturbances (including large thermal gradients and internally induced excitations) that can lead to degraded optical performance, and hence they require active surface control for proper imaging. Active materials such as active fiber composites (AFCs) or piezoceramics have been proposed to provide disturbance rejection; the idea is to attach an appropriate number of actuators along the outer rim of the optical surface (Fig. 1). Furthermore, these actuators can be used to correct for optical aberrations.

Research in the field of large lightweight satellite structures, also known as gossamer structures, has been ongoing since the 1960s. Cassapakis and Thomas [2] presented an overview of the development of inflatable structures through the 1990s. Jenkins [3] provided the most comprehensive coverage of gossamer technology, including topics ranging from the mechanics of membranes to inflatable space habitats. Gorinevsky and Hyde [4] discussed how control of a membrane reflector shape can be achieved using embedded actuators distributed over the membrane surface. Davis and Agnes [5] presented a study of the loads that inflatable space structures encounter when in orbit. Their study focused on the loads that result from the interaction between the satellite and the space environment, such as gravity gradient, aerodynamic drag, solar radiation pressure, magnetic torques, and thermal flux. Rogers and Agnes [6,7] modeled an active optical membrane as a laminate. The membrane was augmented with piezopolymer sheets. The method of integral multiple scales was used to present a nonlinear one-dimensional model. Furthermore, an axisymmetric active membrane was studied. Sobers et al. [8] explored the feasibility of using embedded piezoelectric materials to control polymer optical surfaces. Ruggiero et al. [9] reviewed research conducted in the area of inflatable toroids, with emphasis on experimental modal analysis and the benefits of employing active materials for vibration control. Ruggiero et al. [10] presented a review of the developing research approaches aiming at the shape control of membrane mirrors. Wong and Pellegrino [11] presented a nonlinear finite element simulation technique to accurately predict the wrinkle detail of membrane mirrors. Wong and Pelligrino [12] presented an analytical method to predict wrinkle wavelengths and out-of-plane wrinkle displacement. They considered an idealized solar sail consisting of a uniform, elastic, isotropic square membrane that is prestressed by two pairs of equal and opposite forces applied at the corners. Ruggiero and Inman [13] addressed the issues of wrinkle elimination and membrane

Received 2 October 2006; revision received 17 May 2007; accepted for publication 20 May 2007.

*Graduate Student, Center for Intelligent Material Systems and Structures; renno@vt.edu. Student Member AIAA (Corresponding Author).

†G. R. Goodson Professor and Director, Center for Intelligent Material Systems and Structures. Fellow AIAA.

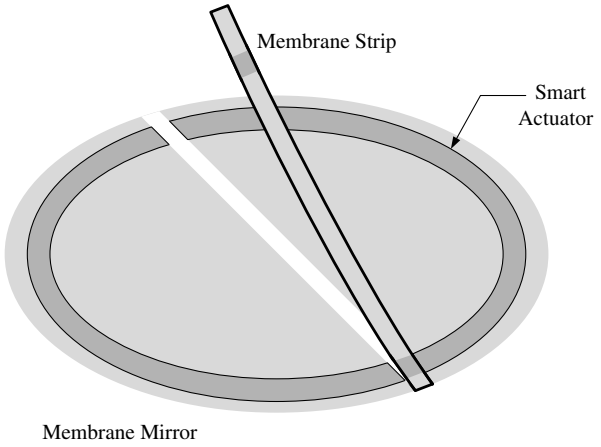

Fig. 1 Schematic of the membrane mirror augmented with a smart actuator around its outer rim.

shape control in gossamer structures; they also provided a summary of recent breakthroughs in gossamer technology and pointed out important gaps in the field. Shepherd et al. [14] presented the construction and testing of a 5-in. in-plane-actuated (using piezoelectric transducer elements), tensioned, deformable mirror. They compared the experimental data with the finite element model (FEM) obtained using commercial software. A control algorithm was implemented based on the finite element model to achieve quasi-static shaping of the mirror surface. Peng et al. [15] used a genetic algorithm to search for the optimal tension that minimizes membrane-mirror wrinkles. The algorithm was tested on a 200 × 300 mm rectangular Kapton membrane. A vision system was developed to measure the membrane flatness under different tension combinations.

The study of image aberrations is a separate and well-developed area in its own right. Many researchers have focused on developing methods to correct for image aberrations. In the area of shape control, Marker and Jenkins [16] proposed achieving shape modification through enforcing boundary displacements, thereby achieving a desired parabolic profile. They performed shape control of an inflated thin circular disk by using nonlinear finite element analysis. Marker et al. [17] examined 75- and 125-μm-thick polyimide films under various strain conditions to show how strain and the optimal optical surface are related. Wilkes et al. [18] presented two methods to achieve optically desirable deterministic shapes. The first method involved prestraining the membrane to reduce the spherical aberrations in such a mirror. The second method involved the use of a plunger to translate the central region of the membrane along the optical axis. Vdovin et al. [19] reported on the progress in the development of a micromachined deformable membrane mirror. The mirror featured a maximum surface deflection of 18 μm and a response time better than 2 ms. Pollard et al. [20] investigated the nonlinear dynamic behavior of membrane mirrors to visible-optics quality under realistic support and loading scenarios. Ruggiero [21] developed a basis for conversing between the optical and mechanical realms. The analysis presented [21] demonstrated that structural characteristics of a circular lens could be used advantageously as an adaptive-optic deformable mirror for eliminating 100% of a fifth-order image aberration. Moore et al. [22] presented their effort in fabricating and testing a 1-m-class lenticular membrane mirror using active boundary control and stress-coating applications to form a usable aperture for visible-imaging applications. Chodimella et al. [23] performed boundary control on a 0.25-m pressure-augmented membrane mirror to correct certain types of figure errors. Patrick et al. [24] presented the final testing data of a 0.7-m-diam mirror using thin-film polymer membranes. Their testing involved the use of a canopy augmented with a reflectively coated membrane. Pressurization was used to establish a desired focal length. Korde et al. [25] used a small number of electrostatic actuators located very close to two opposite boundaries of a rectangular membrane. Green's function was used to model the solution, and the role of the tension within the membrane was examined analytically and experimentally.

This paper proposes augmenting optical membrane mirrors with an appropriate number of actuators along their boundaries, with the hope of eventually controlling optical properties that are not presently addressed. To simplify this approach, this work focuses on the one-dimensional element of a membrane mirror: a membrane strip. Hall et al. [26] presented results of dynamic characterization of thin-film membrane strips. The experimental results were compared with classical closed-form solutions and finite element models. In a previous work, Renno et al. [27] modeled a strip of membrane mirror augmented with a single piezoelectric bimorph. The work of Renno et al. was an improvement upon the model Ruggiero [21] presented for the same structure. The previous model did not include the added mass and flexural rigidity by the piezoceramic bimorph [21]. Renno and Inman [28] presented a model for a membrane-mirror strip augmented with multiple microfiber composite (MFC) actuators. MFCs, a class of AFCs, have less mass and stiffness than traditional piezoceramics and hence are less expected to change the properties of the membrane strip. Wilkie et al. [29] presented the design, manufacturing, and testing of MFC actuators. These actuators use interdigitated electrodes for poling and subsequent actuation of an internal layer of machined piezoceramic fibers. Yet, because the MFC actuators are substantially stiffer than the membrane material, the effects of the MFC actuators on the dynamics of the membrane strip must be modeled to obtain the dynamics of the structure. The mathematical developments presented in [27] will be followed herein.

Hence, this work considers a membrane-mirror strip augmented with two MFC bimorphs. The MFC bimorphs are attached to the membrane strip near its ends. Two configurations are considered in this work. For the first configuration, both bimorphs will act in bending to change the shape of the strip. For the second configuration, one bimorph will act in bending and the other bimorph will act axially to locally change the tension in the structure. The focus of the effort here is to derive and experimentally verify the coupled actuator and structure dynamics and to illustrate the effect of local tension and shape control. This will provide the background for later work to examine if local tension control can be used to improve optical qualities.

In this paper, we look at a new configuration of piezoelements that allows both tension and shape control, whereas previously published work has only addressed shape control and vibration suppression using piezoelements. This configuration of local tension control may lead to improved optical performance once extended to two dimensions and combined with the Zernike polynomial description used in adaptive optics [30,31].

The rest of this paper is arranged as follows. Section II presents a model of the structure in the two configurations. An experimental setup to verify the model is presented in Sec. III. Conclusions for this work are drawn in Sec. IV.

II. Dynamic Model

The membrane strip will be modeled as a pinned–pinned Euler–Bernoulli beam under tension [27,32]. The structure (Fig. 2) is modeled as a beam because of the added stiffness of the MFC bimorphs. The bimorphs are placed near the boundaries. The membrane strip cannot resist bending moment, and hence the boundary condition of the structure is pinned–pinned.

The added bimorphs will increase the flexural rigidity of the structure, albeit locally, justifying the beam assumption. Being under tension adds a traveling wave term, usually appearing in the governing equation of a string [21]. Assuming perfect bonding between the bimorph and the membrane, the bimorphs and the membrane will undergo the same strain. Consequently, the equation of motion of the structure can be expressed as [21,28]

$$\rho(x)\frac{\partial^2 w(x,t)}{\partial t^2}+\frac{\partial^2 M_x(x,t)}{\partial x^2}-\frac{\partial}{\partial x}\left(\tau(x,t)\frac{\partial w(x,t)}{\partial x}\right)+\gamma\frac{\partial w(x,t)}{\partial t}=f(x,t) \tag{1}$$

where $\rho(x)$ is the linear density of the structure, $M_x(x,t)$ is the internal bending moment in the structure, $f(x,t)$ is the local bending moment exerted by the MFC actuator(s), and $w(x,t)$ is the transverse deflection of the structure. The tension within the structure is given by $\tau(x,t)$. To capture the effect of the actuator mass, the linear density of the structure is given by

$$\rho(x)=\rho_m hb+\sum_{k=1}^{2}2\rho_k h_k b_k \chi_k(x) \tag{2}$$

where $\chi_k(x)$ is the family of functions characterizing the discontinuity of the physical properties in the structure, defined as

$$\chi_k(x)=\begin{cases}1 & \text{if } x_{2k-1}\le x\le x_{2k}\\ 0 & \text{otherwise}\end{cases}\qquad k=1,2 \tag{3}$$

The internal bending moment is given by

$$M_x(x,t)=EI(x)\frac{\partial^2 w(x,t)}{\partial x^2}+cI(x)\frac{\partial^3 w(x,t)}{\partial t\partial x^2} \tag{4}$$

where $EI(x)$ is the flexural rigidity of the structure. To capture the effect of the MFC stiffness, the flexural rigidity is given by

$$EI(x)=\frac{1}{12}bh^3E+\sum_{k=1}^{2}\frac{2}{3}a_k b_k E_k \chi_k(x) \tag{5}$$

The proper Kelvin–Voigt damping coefficient multiplied by the respective area moment of inertia is

$$cI(x)=\frac{1}{2}bh^3c_D+\sum_{k=1}^{2}\frac{2}{3}c_k a_k b_k \chi_k(x) \tag{6}$$

The bimorph constant [33] a_k is given by

$$a_k=(\tfrac{1}{2}h+h_k)^3-(\tfrac{1}{2}h_k)^3 \tag{7}$$

Finding an exact solution for the governing equation (1) is a formidable task. Approximate methods of analysis provide a convenient alternative for finding the solution. In the following, we adopt a variational method to solve Eq. (1).

A. Weak-Form Formulation

In the sequel, the subscripts t and x will denote partial differentiation with respect to the temporal and spatial variables, respectively. Rewriting the governing equation in a more compact form,

$$\rho(x)w_{tt}(x,t)+[EI(x)w_{xx}(x,t)+cI(x)w_{xxt}(x,t)]_{xx}-[\tau(x,t)w_x(x,t)]_x+\gamma w_t(x,t)=f(x,t) \tag{8}$$

The configuration of the structure can be described by two states, position and velocity, and hence Eq. (8) can be written as

$$\begin{aligned}&w_t(x,t)=v(x,t)\\&\rho(x)v_t(x,t)=f(x,t)+[\tau(x,t)w_x(x,t)]_x\\&\quad-[EI(x)w_{xx}(x,t)+cI(x)v_{xx}(x,t)]_{xx}-\gamma v(x,t)\end{aligned} \tag{9}$$

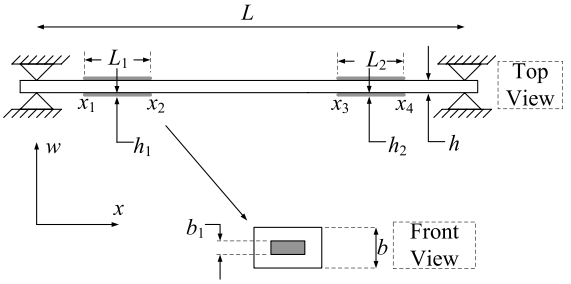

Fig. 2 Schematic of the membrane strip with MFC bimorphs.

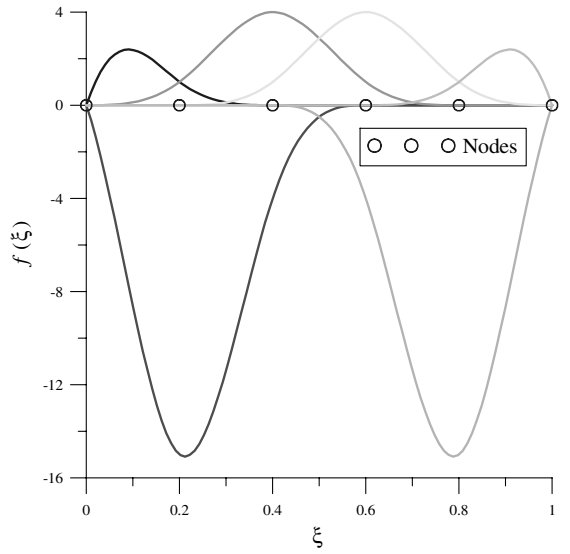

Fig. 3 Cubic B-splines extending over five elements with pinned–pinned boundary conditions.

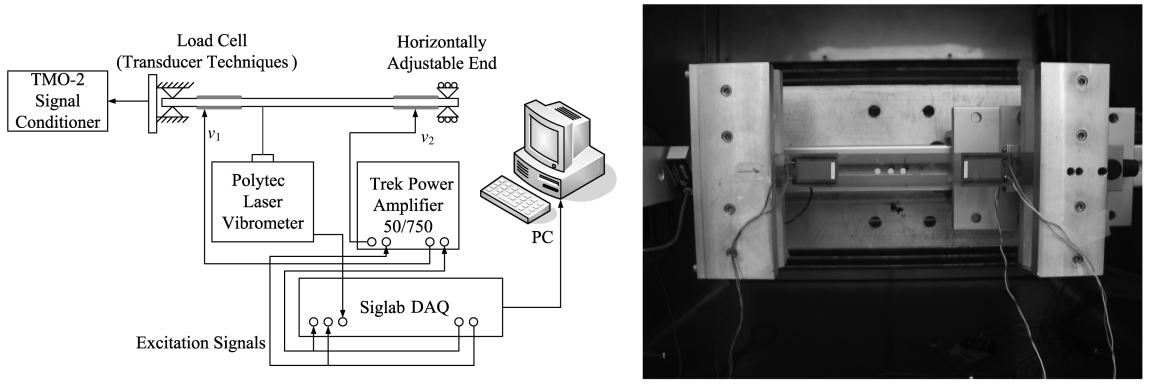

a) Schematic of experimental setup

b) Photo of the test article

Fig. 4 Schematic of the experimental setup (DAQ indicates data acquisition).

Table 1 Properties of Kapton strip and MFC patch for configuration 1

Property	Kapton strip	MFC patch
Density, kg/m^3	1420	994
Young's modulus, GPa	3	34.5
Width, cm	2.5	2.5
Thickness, mm	51×10^{-3}	0.3
Length, cm	18	3.8

Notice that $EI(x)$ and $cI(x)$ have to be differentiated twice, which gives rise to

$$\chi_{kxx}(x) = [H(x - x_{2k}) - H(x - x_{2k-1})]_{xx} = [\delta(x - x_{2k}) - \delta(x - x_{2k-1})]_x \tag{10}$$

where $H(x)$ is the Heaviside function and $\delta(x)$ is the Dirac delta function. The strong form of Eq. (9) can lead to computational difficulties for estimation and control applications. Banks et al. [34] showed that the retention of the irregular terms of Eq. (10) is of great importance when using models with experimental data from actual structures.

To formulate the weak form of Eq. (9), multiply each equation by test functions $\phi(x)$ and $\psi(x)$:

$$w_t(x,t)\phi(x) = v(x,t)\phi(x) \tag{11}$$

$$\rho(x)v_t(x,t)\psi(x) = \{f(x,t) + [\tau(x,t)w_x(x,t)]_x - [EI(x)w_{xx}(x,t) + cI(x)v_{xx}(x,t)]_{xx} - \gamma v(x,t)\}\psi(x) \tag{12}$$

Integrate both equations spatially over the domain of application (the length of the strip):

$$\int_0^L \frac{\partial w(x,t)}{\partial t}\phi(x)\,\mathrm{d}x = \int_0^L v(x,t)\phi(x)\,\mathrm{d}x \tag{13}$$

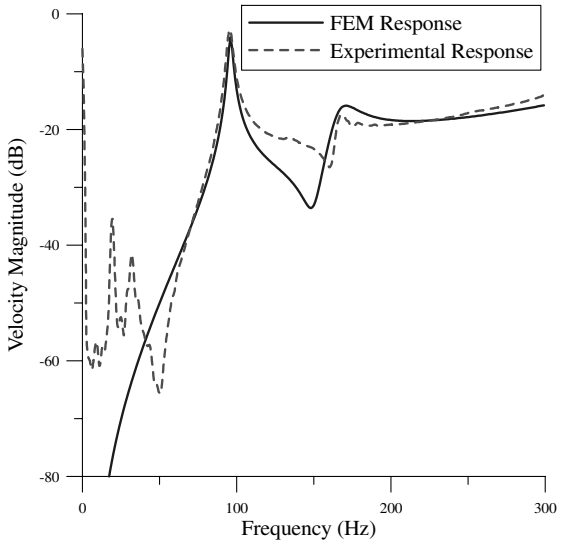

a) Frequency response with V_1 as input

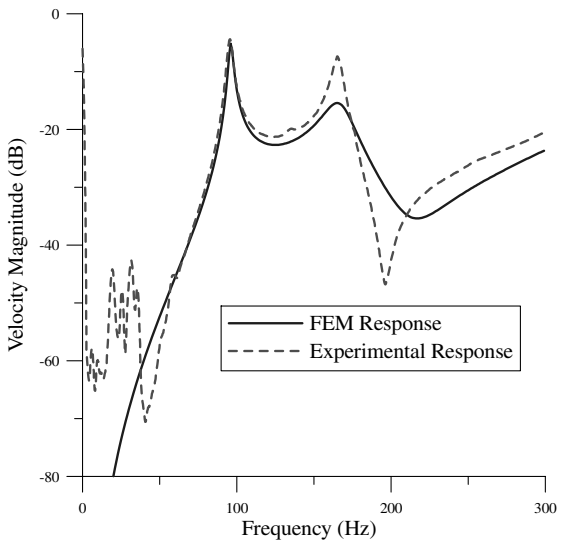

b) Frequence response with V_2 as input

Fig. 5 FEM vs experimental frequency response.

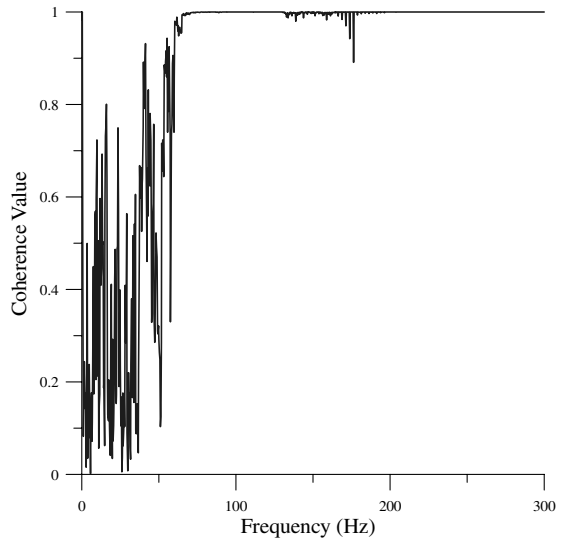

a) Coherence of results with V_1 as input

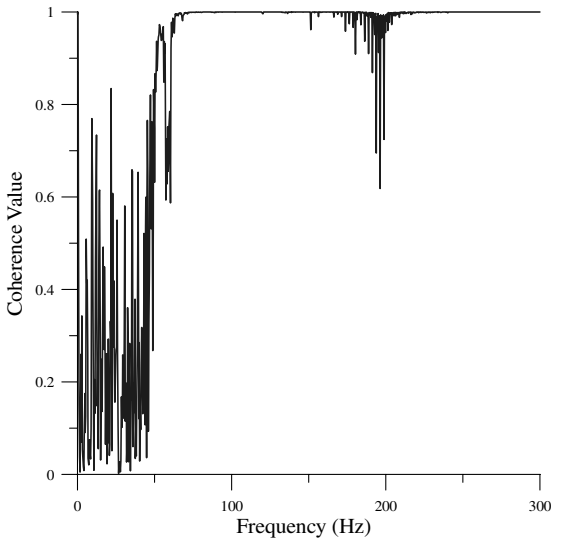

b) Coherence of results with V_2 as input

Fig. 6 Coherence of experimental results.

Table 2 Frequencies of the structure tested for configuration 1

Frequency	FEM, Hz	Experimental, Hz	Error, %
f_1	96.05	95.6	0.47
f_2	165.25	163.35	1.16
f_3	170.65	168.5	1.28

Table 3 Properties of Kapton strip and MFC patch: configuration 2

Property	Kapton strip	Mfc patch
Density, kg/m^3	1420	994
Young's modulus, GPa	3	34.5
Width, cm	2.5	2.5
Thickness, mm	51×10^{-3}	0.3
Length, cm	22	3.8

$$\int_0^L \rho(x)\frac{\partial v(x,t)}{\partial t}\psi(x)\,\mathrm{d}x = \int_0^L (f(x,t) + [\tau(x,t)w_x(x,t)]_x - [EI(x)w_{xx}(x,t) + cI(x)v_{xx}(x,t)]_{xx} - \gamma v(x,t))\psi(x)dx \quad (14)$$

Following the derivation of Renno et al. [27], the state equations become

$$\frac{\partial}{\partial t}\int_0^L w(x,t)\phi(x)\,\mathrm{d}x = \int_0^L v(x,t)\phi(x)\,\mathrm{d}x \quad (15)$$

$$\frac{\partial}{\partial t}\int_0^L \rho(x)v(x,t)\psi(x)\,\mathrm{d}x = \int_0^L f(x,t)\psi(x)\,\mathrm{d}x - \int_0^L \tau(x,t)w_x(x,t)\psi_x(x)\,\mathrm{d}x - \int_0^L [EI(x)w_{xx}(x,t) + cI(x)v_{xx}(x,t)]\psi_{xx}(x)\,\mathrm{d}x - \gamma\int_0^L v(x,t)\psi(x)\,\mathrm{d}x \quad (16)$$

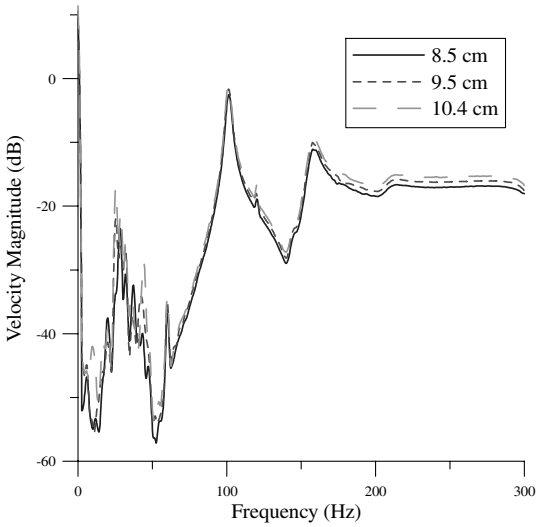

a) Frequency response

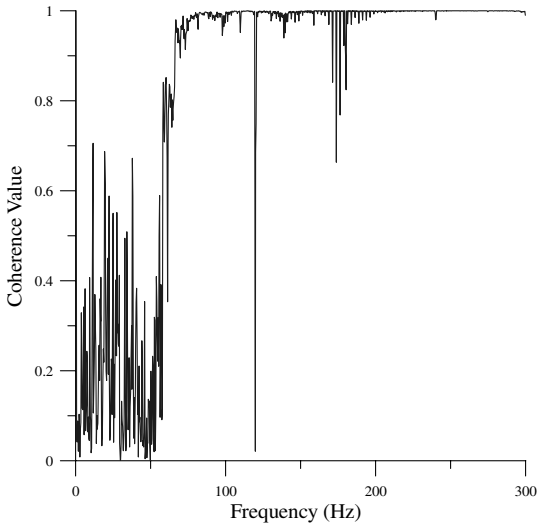

b) Coherence for measurements at 8.5 cm

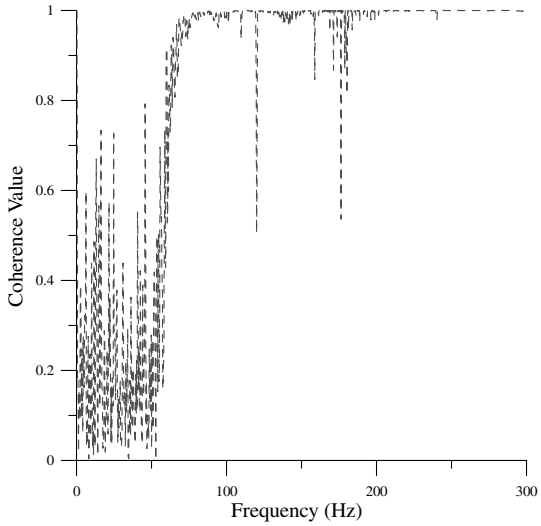

c) Coherence for measurements at 9.5 cm

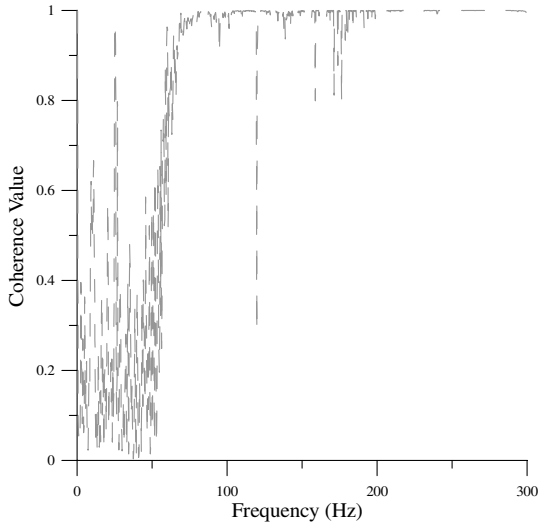

d) Coherence for measurements at 10.4 cm

Fig. 7 Experimental frequency response obtained at various measurement points.

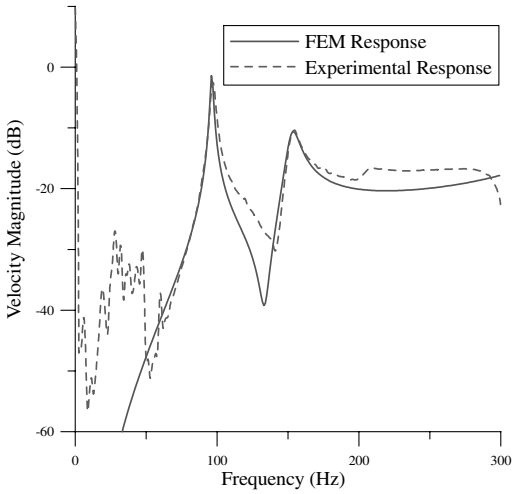

a) Frequency response with V_2=0 V

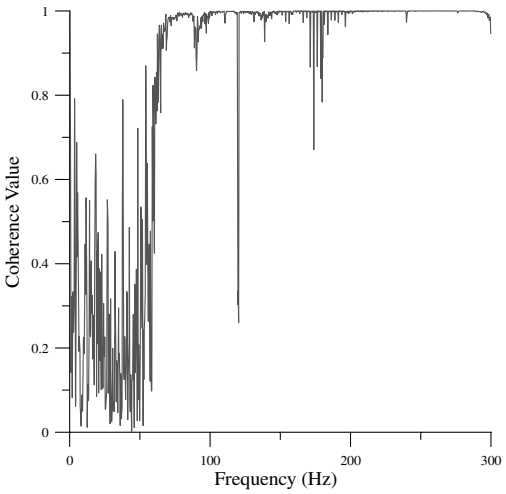

b) Coherence with V_2=0 V

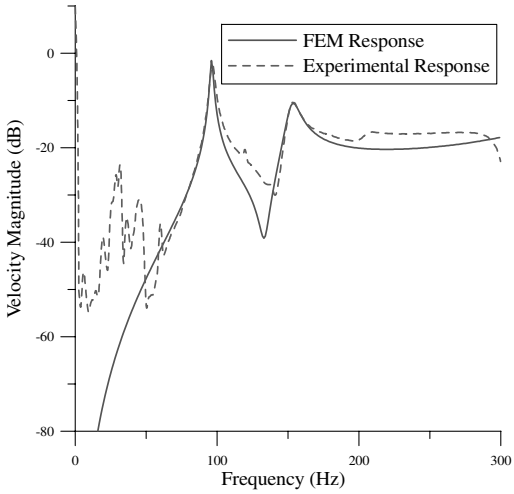

c) Frequence response with V_2=75 V

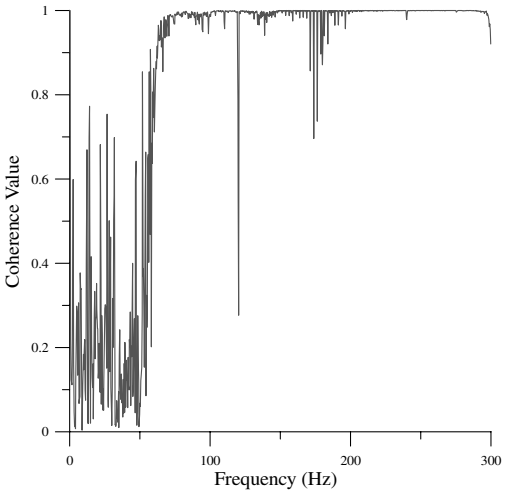

d) Coherence with V_2=75 V

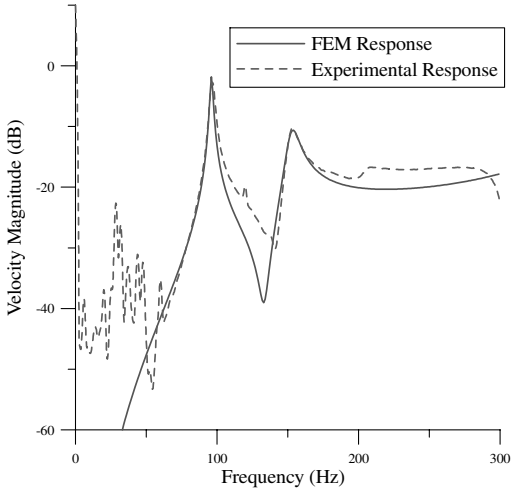

e) Frequency response with V_2=150 V

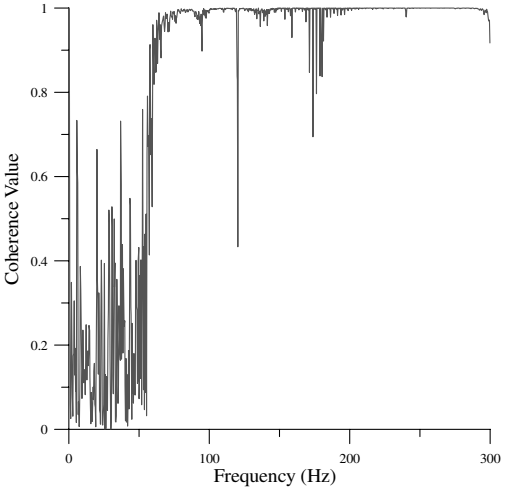

f) Coherence with V_2=150 V

Fig. 8 FEM vs experimental frequency response with nominal tension $\bar{\tau} = 8$ N.

Now approximate the transverse deformation of the structure as the summation of the product of temporal and spatial functions:

$$w(x,t) = \sum_{i=1}^{N} \bar{w}_i(t)\phi_i(x) \tag{17}$$

$$v(x,t) = \sum_{i=1}^{N} \bar{v}_i(t)\psi_i(x) \tag{18}$$

Notice that the test functions $\phi(x)$ and $\psi(x)$ are dummy functions yet to be determined. Because $\phi(x)$ and $\psi(x) \in H^2(0, L)$, which is the

same Hilbert space, we can let $\phi(x) = \psi(x)$. Consequently, they can be taken from the same functional space. Substituting the approximation equations (17) and (18) into Eqs. (15) and (16) yields

$$\begin{aligned}
&\frac{\partial}{\partial t}\sum_{i=1}^{N}\bar{w}_i(t)\int_0^L \phi_i(x)\phi_j(x)\,\mathrm{d}x = \sum_{i=1}^{N}\bar{v}_i(t)\int_0^L \phi_i(x)\phi_j(x)\,\mathrm{d}x\\
&\frac{\partial}{\partial t}\sum_{i=1}^{N}\bar{v}_i(t)\int_0^L \phi_i(x)\phi_j(x)\,\mathrm{d}x\\
&\quad = \int_0^L f(x,t)\psi(x)\,\mathrm{d}x - \sum_{i=1}^{N}\bar{w}_i(t)\int_0^L \tau(x,t)\phi_i'(x)\phi_j'(x)\,\mathrm{d}x\\
&\quad - \sum_{i=1}^{N}\bar{w}_i(t)\int_0^L EI(x)\phi_i''(x)\phi_j''(x)\,\mathrm{d}x\\
&\quad - \sum_{i=1}^{N}\bar{v}_i(t)\int_0^L cI(x)\phi_i''(x)\phi_j''(x)\,\mathrm{d}x\\
&\quad - \gamma\sum_{i=1}^{N}\bar{v}_i(t)\int_0^L \phi_i(x)\phi_j(x)\,\mathrm{d}x
\end{aligned} \tag{19}$$

The structure of Eq. (19) depends on the nature of actuation used. Recall that this work proposes two actuation configurations. In the following, Eq. (19) will yield two models for the structure, depending on the configuration pursued. To this end, cast Eq. (19) in matrix form:

$$\begin{bmatrix} M_1 & 0_{N\times N} \\ 0_{N\times N} & M_2 \end{bmatrix}\begin{Bmatrix}\dot{\bar{w}}\\ \dot{\bar{v}}\end{Bmatrix}_t = \begin{bmatrix} 0_{N\times N} & M_1 \\ -K(t) & -C \end{bmatrix}\begin{Bmatrix}\bar{w}\\ \bar{v}\end{Bmatrix} + F(t) \tag{20}$$

The submatrices are defined as

$$\begin{aligned}
M_1 &= \left[\int_0^L \phi_i(x)\phi_j(x)\,\mathrm{d}x\right]_{i,j=1,\cdots,N}\\
M_2 &= \left[\int_0^L \rho(x)\phi_i(x)\phi_j(x)\,\mathrm{d}x\right]_{i,j=1,\cdots,N}\\
F(t) &= \left[\int_0^L f(x,t)\phi_j(x)\,\mathrm{d}x\right]_{(j=1,\cdots,N)}\\
K(t) &= \left[\int_0^L \left(EI(x)\phi_i''(x)\phi_j''(x) + \tau(x,t)\phi_i'(x)\phi_j'(x)\right)\mathrm{d}x\right]_{i,j=1,\cdots,N}\\
C &= \left[\int_0^L \left(cI(x)\phi_i''(x)\phi_j''(x) + \gamma\phi_i(x)\phi_j(x)\right)\mathrm{d}x\right]_{i,j=1,\cdots,N}
\end{aligned} \tag{21}$$

Notice that the stiffness matrix $K(t)$ can be time-dependent, because the tension might be time-varying. This idea will be explored more in the following subsections.

B. Configuration 1: Bending–Bending

For configuration 1, both bimorphs will be acting in bending. In this case, the forcing function on the right side of Eq. (1) will be

$$f(x,t) = -\sum_{k=1}^{2}\frac{\partial^2[M_x(x,t)]_k}{\partial x^2} \tag{22}$$

where $[M_x(x,t)]_k$ is the bending moment exerted by the kth bimorph [35], defined as

$$[M_x(x,t)]_k = -2\kappa_k^B\chi_k(x)V_k(t) \tag{23}$$

where κ_k^B is the bending constant of the kth bimorph [35]. Substituting Eq. (23) into Eq. (19) and following the developments of [34] yields

$$F(t) = \sum_{k=1}^{2}2\kappa_k^B V_k(t)\int_0^L \chi_k(x)\phi_j''(x)\,\mathrm{d}x = \sum_{k=1}^{2}\begin{bmatrix}0_{N\times 1}\\ B_k\end{bmatrix}V_k(t) \tag{24}$$

where B_k is the $N\times 1$ input vector corresponding to the kth bimorph, defined as

$$B_k = \left[2\kappa_k^B\int_0^L \chi_k(x)\phi_j''(x)\,\mathrm{d}x\right]_{(k=1,2),(j=1,\cdots,N)} \tag{25}$$

Regarding the tension, there is no actuation in the axial direction, and hence the tension is not time-varying. Moreover, it was shown that the tension is constant along the structure [28]. Consequently, the stiffness matrix is constant. Based on these developments, Eq. (20) reduces to

$$\begin{aligned}
\begin{Bmatrix}\dot{\bar{w}}\\ \dot{\bar{v}}\end{Bmatrix}_t &= \begin{bmatrix} 0_{N\times N} & I_{N\times N} \\ -M_2^{-1}K & -M_2^{-1}C \end{bmatrix}\begin{Bmatrix}\bar{w}\\ \bar{v}\end{Bmatrix}\\
&+ \begin{bmatrix} 0_{N\times 1} & 0_{N\times 1} \\ M_2^{-1}B_1 & M_2^{-1}B_2 \end{bmatrix}\begin{Bmatrix}V_1(t)\\ V_2(t)\end{Bmatrix}
\end{aligned} \tag{26}$$

Equation (26) presents a multi-input/multi-output linear system. Linear control techniques can be used to perform shape control of this structure.

C. Configuration 2: Bending–Tension

Configuration 2 uses an alternative approach. One of the bimorphs is actuated in bending (BMFC), whereas the other bimorph is actuated axially (AMFC). Hence, the tension within the structure is not constant anymore. The tension varies temporally as the applied voltage varies. Moreover, the tension changes at the location of the AMFC bimorph. The tension is defined as

$$\tau(x,t) = \bar{\tau} + 2\kappa_2^A S_{3,4}(x)\chi_2(x)V_2(t) \tag{27}$$

The second term in Eq. (27) stands for the axial load exerted by applying voltage to the AMFC bimorph, and κ_2^A is the axial constant of the AMFC bimorph [35]. The function $S_{3,4}(x)$ characterizes the actuation of AMFC and is given by

$$S_{3,4}(x) = \begin{cases} 1 & \text{if } x < (x_3 + x_4)/2\\ 0 & \text{if } x = (x_3 + x_4)/2\\ -1 & \text{if } x > (x_3 + x_4)/2 \end{cases} \tag{28}$$

Understanding the nature of $\chi_2(x)$ and $S_{3,4}(x)$ turns out to be crucial to understand the behavior of the structure when using configuration 2. The function $\chi_2(x)$ points to structural attributes. It implies the presence of the bimorph regardless of its actuation nature (bending/tension). On the other hand, $S_{3,4}(x)$ is related to the actuation attributes. It simply says that for a positive voltage, opposite but equal strains are generated about the midpoint of the bimorph.

For configuration 2, the stiffness matrix $K(t)$ of Eq. (21) becomes

$$\begin{aligned}
K(t) = \Bigg(&\int_0^L \{EI(x)\phi_i''(x)\phi_j''(x)\\
&+ [\bar{\tau} + 2\kappa_2^A S_{3,4}(x)\chi_2(x)V_2(t)]\phi_i'(x)\phi_j'(x)\}\,\mathrm{d}x\Bigg) i,j = 1,\cdots,N
\end{aligned} \tag{29}$$

For the scope of this work, $V_2(t)$ is assumed to be constant so that the stiffness matrix defined in Eq. (29) will be constant and the system will be linear. Modeling the BMFC is treated as in [27], and hence the equations of motion for configuration 2 become

$$\begin{Bmatrix}\dot{\bar{w}}\\ \dot{\bar{v}}\end{Bmatrix}_t = \begin{bmatrix} 0_{N\times N} & I_{N\times N} \\ -M_2^{-1}K & -M_2^{-1}C \end{bmatrix}\begin{Bmatrix}\bar{w}\\ \bar{v}\end{Bmatrix} + \begin{bmatrix}0_{N\times 1}\\ M_2^{-1}B_1\end{bmatrix}V_1(t) \tag{30}$$

The input vector B_1 is given in Eq. (25).

D. Finite Element Formulation

The FEM is known for its computational efficiency. This is due to the symmetrical banded nature of the developed system matrices M_2, K, and C of Eq. (20). Additionally, the FEM is an approximate

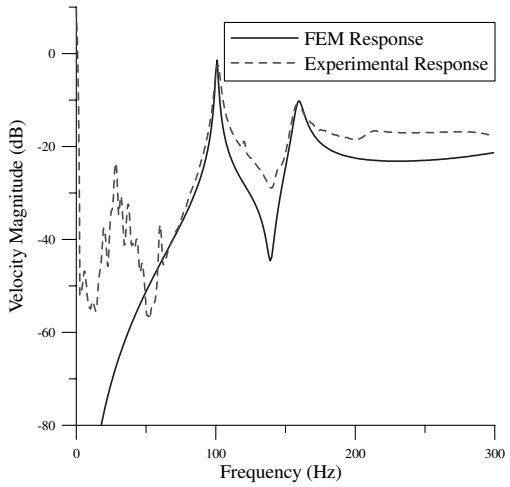

a) Frequency response with V_2=0 V

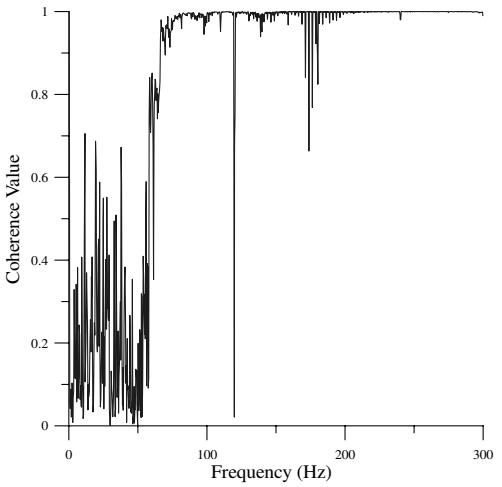

b) Coherence with V_2=0 V

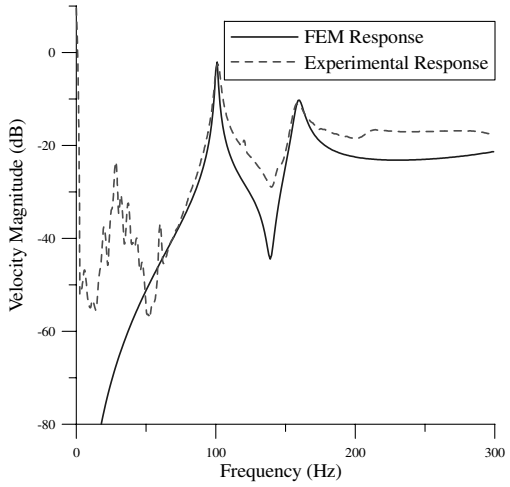

c) Frequence response with V_2=75 V

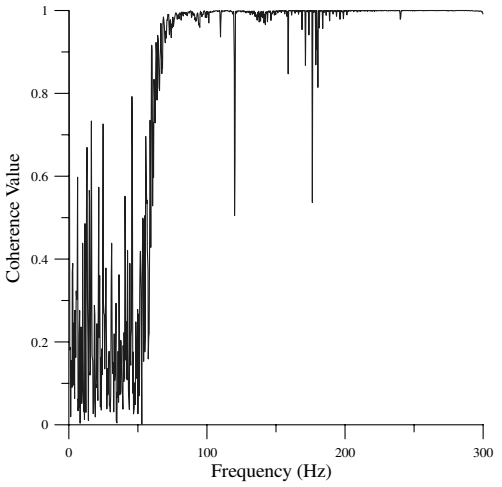

d) Coherence with V_2=75 V

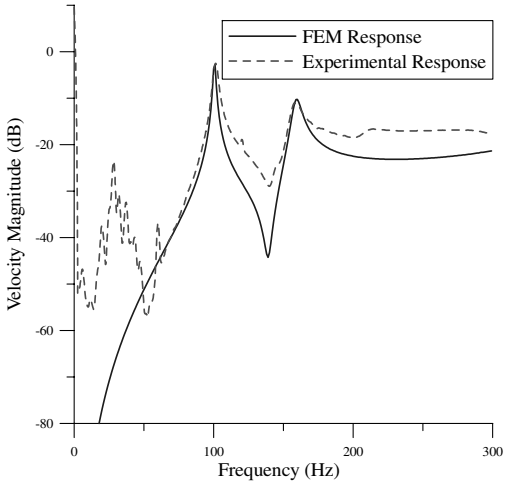

e) Frequency response with V_2=150 V

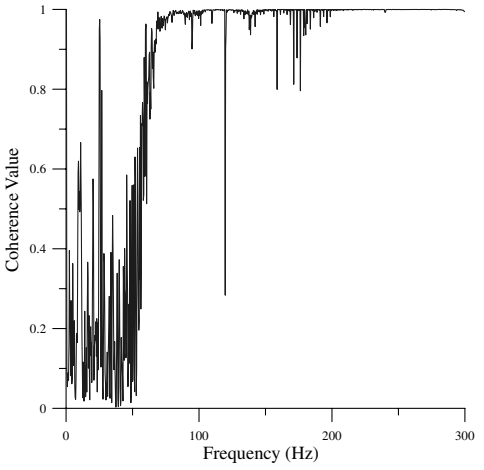

f) Coherence with V_2=150 V

Fig. 9 FEM vs experimental frequency response with nominal tension $\bar{\tau} = 10$ N.

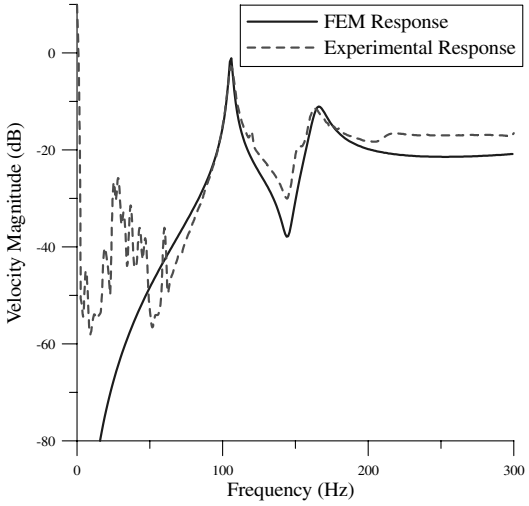

a) Frequency response with V_2=0 V

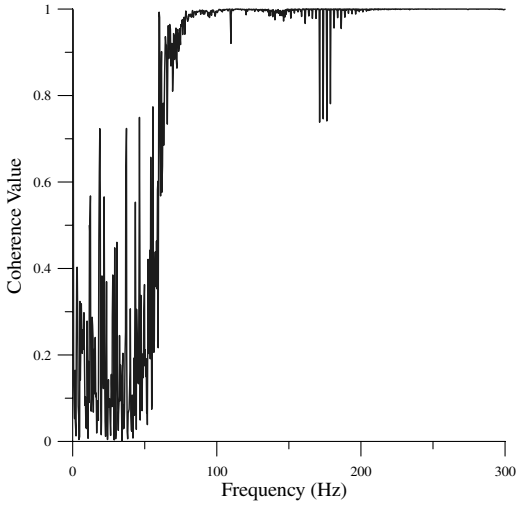

b) Coherence with V_2=0 V

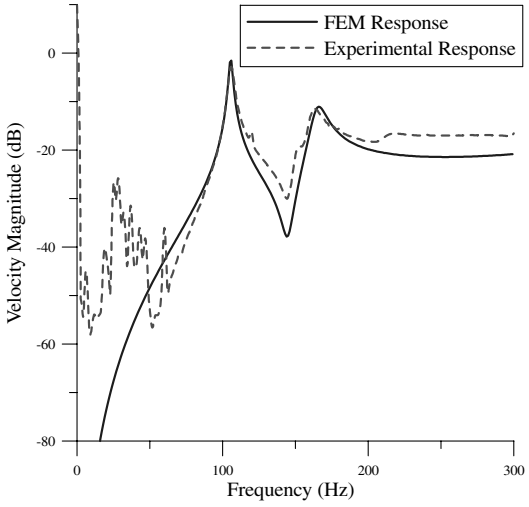

c) Frequence response with V_2=75 V

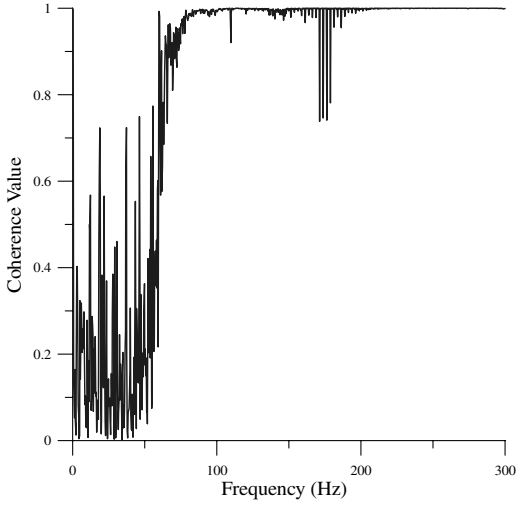

d) Coherence with V_2=75 V

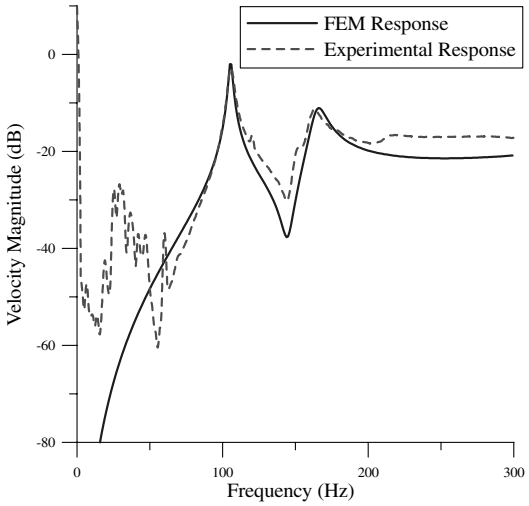

e) Frequency response with V_2=150 V

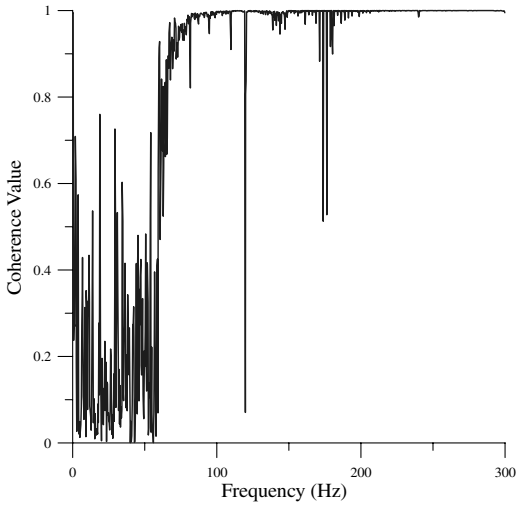

f) Coherence with V_2=150 V

Fig. 10 FEM vs experimental frequency response with nominal tension $\bar{\tau} = 12$ N.

approach for developing a control law for distributed systems [36]. When used, the FEM yields a finite dimensional representation of a system with an infinite number of degrees of freedom. Although many commercial packages are available, careful design of a tailored finite element solver can reveal information about the system, such as where sensors should be placed on the structure. In this spirit, a custom finite element code is devised for this work.

For this work, the test functions used are cubic B-splines. Cubic B-splines are a set of linearly independent functions that form a basis for the finite element approximation. The following presents a cubic B-spline extending over four elements [37]:

$$e_i^{-3} f(\xi) = \begin{cases} (\xi - \xi_{i-2})^3 & \text{if } \xi_{i-2} \le \xi \le \xi_{i-1} \\ e_i^3 + 3e_i^2(\xi - \xi_{i-1}) + 3e_i(\xi - \xi_{i-1})^2 - 3(\xi - \xi_{i-1})^3 & \text{if } \xi_{i-1} \le \xi \le \xi_i \\ e_i^3 + 3e_i^2(\xi_{i+1} - \xi) + 3e_i(\xi_{i+1} - \xi)^2 - 3(\xi_{i+1} - \xi)^3 & \text{if } \xi_i \le \xi \le \xi_{i+1} \\ (\xi_{i+2} - \xi)^3 & \text{if } \xi_{i+1} \le \xi \le \xi_{i+2} \\ 0 & \text{otherwise} \end{cases} \tag{31}$$

where ξ_i and ξ_{i+1} are the nodes of the ith element of length e_i. Cubic B-splines exhibit high connectivity among the discretized structure, because every B-spline extends over the range of four elements. Figure 3 displays a set of cubic B-splines for a structure discretized into five elements. De Boor et al. [38] discussed cubic B-splines extensively. Hollig [39] also presented several types of B-spline basis for approximation and boundary-value problems and discussed the implementation of spline-based finite element schemes.

The structure under study (Fig. 2) is discretized into 256 elements. Cubic B-splines with pinned–pinned boundary conditions, similar to Fig. 3, are used to span the space for the FEM approximation.

III. Experimental Validation

An experiment is used to verify the model presented in Sec. II. A membrane strip made of Kapton, a polyimide that has been a commonly used membrane material for recent space applications [1], is considered. The MFC patches (M-2814-P1) are made by Smart Materials Corporation. Figure 4a shows a schematic of the experimental setup. The Kapton strip is held between two grippers. The left gripper remains fixed, and the right gripper's position is adjustable through the lead screw displayed in Fig. 4b to produce a tensile load in the structure. A MLP-75 load cell by Transducer Techniques is used to measure the tension in the structure. While exciting the structure, the right gripper can be fixed to its position via a setscrew. In other words, the right gripper is only used to tension the structure, and the structure is under pinned–pinned boundary conditions when excited. A Polytec laser vibrometer (OFV 303) is used to measure the velocity of a single point on the centerline of the Kapton strip. The laser vibrometer shines a laser on the structure. The reflection of the laser beam is used to measure the velocity of the structure at that point. Kapton has poor reflective properties, and small pieces of highly reflective tape are therefore placed along the centerline of the test article.

The structure is excited through Siglab by Spectral Dynamics. Siglab is also used to construct the frequency response of the structure. For all of the tests presented hereafter, the excitation signal is a burst-chirp signal that is generated every other second. The chirp signal sweeps the frequencies between 0.01 and 300 Hz in 1 s. The frequency resolution is 0.3125 Hz. After every excitation, the frequency response is constructed. The structure is excited 10 times, and the measurements collected are averaged. The average measurement is compared with the FEM prediction. A Trek, Inc. amplifier (model 50/750) is used to amplify the excitation signal by a factor of 20.

The frequency values predicted by the FEM are compared with the experimental values. The percentage errors are calculated using

$$\text{error } \% = \frac{|f_{\text{ex}} - f_{\text{fe}}|}{f_{\text{ex}}} \times 100 \tag{32}$$

and are also listed next for all of the tests conducted.

A. Treating the Bonding Issue: Vacuum Bagging

The derivation of Eq. (1) assumes perfect bonding between the membrane strip and the MFC patches. The assumption of perfect bonding implies that both the membrane strip and the MFC patches experience the same strain. To achieve near-perfect bonding between the membrane strip and the MFC patches, vacuum bagging is used. Vacuum bagging is a technique widely used when manufacturing composite materials.

To implement this technique, an aluminum plate is used as a working surface. A rectangle is constructed on the surface using sticky sealant (GS 27) by General Sealants around the section in which the MFC will be bonded to the membrane strip. Cyanoacrylate adhesive by Handibond is applied to the membrane strip and the MFC patch. A vacuum bag (GS A-800-3G) by General Sealants is placed atop the sticky sealant. The tube of a vacuum pump is augmented with a syringe that is inserted in the sealant. A vacuum pump evacuates the sealed chamber. This technique eliminates the need to place weights atop the MFC until the adhesive cures. By removing the air from inside the bag, the atmospheric pressure acts against the bag, pressing the MFC against the membrane strip. This pressure is applied evenly and perpendicularly to all surfaces inside the bag.

B. Experimental Validation of Configuration 1

For configuration 1, both bimorphs are excited in bending. The burst-chirp signal had a peak amplitude of 0.5 V. The actuators were excited one at a time. Table 1 shows the physical properties of the structure that was tested in this configuration. The first bimorph is placed at $x_1 = 3.2$ cm and the second bimorph is placed at $x_3 = 14$ cm. The tension in the structure was set to 8 N.

Figure 5 displays the frequency response obtained via the experimental setup and that was predicted by the FEM. Table 2 lists the results for the natural frequencies. The error did not exceed 2%. Recall that the experimental frequency response viewed in Fig. 5 is the average of ten measurements. Figure 6 shows the coherence of the measurements.

The first frequency f_1 is excited with both inputs. On the other hand, f_2 was only excited with the first input V_1, and f_3 was only excited with the second input V_2.

C. Experimental Validation of Configuration 2

As discussed in Sec. II, the voltage supplied to the AMFC is kept constant during each test, to obtain a linear model. Three values of nominal tension $\bar{\tau}$ are applied to the structure: 8, 10, and 12 N

[Eq. (27)]. The BMFC was placed at $x_1 = 2.5$ cm and the AMFC was placed at $x_3 = 15.2$ cm (Fig. 2). The physical properties of the test article tested for this configuration are given in Table 3.

For each nominal tension value, three voltage values are supplied to the AMFC: 0, 75, and 150 V. For each combination of nominal tension $\bar{\tau}$ and voltage input to AMFC V_2, the structure is excited through the BMFC and the frequency response is obtained, as explained previously. The peak amplitude of the chirp signal used for this configuration is 0.1 V. In total, nine combinations are tested.

Figure 7 shows the frequency response measured at three locations along the centerline of the test article: 8.5, 9.5, and 10.4 cm [all measured from the left boundary (Fig. 4b)]. The coherence of each measurement set is displayed as well. Figures 8–10 show the frequency response of the structure for the nine combinations mentioned earlier. The coherence corresponding to each measurement set is shown as well.

Tables 4–6 list the FEM predictions and the experimentally obtained values of the frequencies. The percentage error is calculated using Eq. (32). The percentage error did not exceed 2% for all of the values obtained.

Examining the results reveals the following. When no voltage is supplied to the AMFC (i.e., $V_2 = 0$), the frequency response shifts to higher values as the nominal tension increases. This can be predicted if one examines Eq. (29). Simply, increasing the tension increases the stiffness, which in turn causes an increase of the frequency values.

Now consider the results obtained of the cases in which a nonzero voltage is applied to the AMFC (i.e., $V_2 = 75$ and 150 V). The frequency response for these two cases shifted to lower values as the value of V_2 increased. The increase in V_2 causes a decrease in tension [Eq. (27)] at the location of the AMFC. Figure 11 shows the characteristic function that describes the behavior of the AMFC bimorph. With positive values of V_2, the AMFC equally expands in both directions, with its midpoint being stationary. This behavior relieves some of the axial load placed on the membrane strip through the nominal tension at the location of the AMFC. As such, this creates

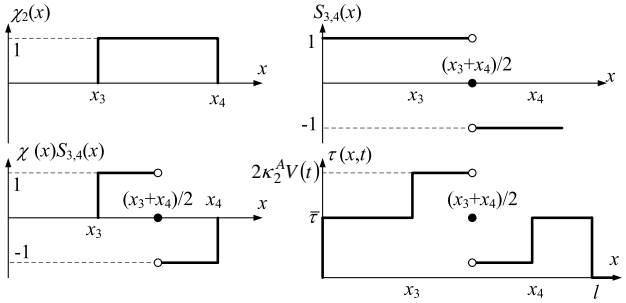

Fig. 11 Tension characteristic functions.

a softening behavior, which yields to lower frequency values as V_2 increases.

Moreover, the effect of the AMFC is dependent upon its size and location. This can be clearly observed if one expands Eq. (27):

$$K(t) = \left[\int_0^L EI(x)\phi_i''(x)\phi_j''(x)\,\mathrm{d}x\right]_{i,j=1,\cdots,N} + \bar{\tau}\left[\int_0^L \phi_i''(x)\phi_j''(x)\,\mathrm{d}x\right]_{i,j=1,\cdots,N} + 2\kappa_2^A V_2\left[\int_0^L S_{3,4}(x)\chi_2(x)\phi_i''(x)\phi_j''(x)\,\mathrm{d}x\right]_{i,j=1,\cdots,N} \tag{33}$$

where the last term of Eq. (33) can be further expanded as

$$\int_0^L S_{3,4}(x)\chi_2(x)\phi_i''(x)\phi_j''(x)\,\mathrm{d}x = \int_{x_3}^{(\frac{x_3+x_4}{2})^-} \phi_i''(x)\phi_j''(x)\,\mathrm{d}x - \int_{(\frac{x_3+x_4}{2})^+}^{x_4} \phi_i''(x)\phi_j''(x)\,\mathrm{d}x$$

Table 4 Frequency values of FEM vs experimental results with nominal tension $\bar{\tau} = 8$ N

AMFC voltage, V	Frequency, Hz	FEM result	Experimental result	Error, %
0	f_1	95.85	97.25	1.44
	f_2	153.82	154.95	0.73
75	f_1	94.55	96.36	1.88
	f_2	153.42	154.23	0.53
150	f_1	93.95	95.25	0.73
	f_2	153.40	153.15	0.16

Table 5 Frequency values of FEM vs experimental results with nominal tension $\bar{\tau} = 10$ N

AMFC voltage, V	Frequency, Hz	FEM result	Experimental result	Error, %
0	f_1	100.95	101.35	0.39
	f_2	159.55	157.55	1.26
75	f_1	100.30	100.80	0.49
	f_2	158.80	157.15	1.05
150	f_1	99.53	100.12	0.58
	f_2	158.10	156.62	0.94

Table 6 Frequency values of FEM vs experimental results with nominal tension $\bar{\tau} = 12$ N

AMFC voltage, V	Frequency, Hz	FEM result	Experimental result	Error, %
0	f_1	105.90	105.65	0.23
	f_2	165.80	163.05	1.68
75	f_1	104.82	104.80	0.09
	f_2	164.90	161.90	1.86
150	f_1	104.10	104.65	0.53
	f_2	163.98	161.55	1.51

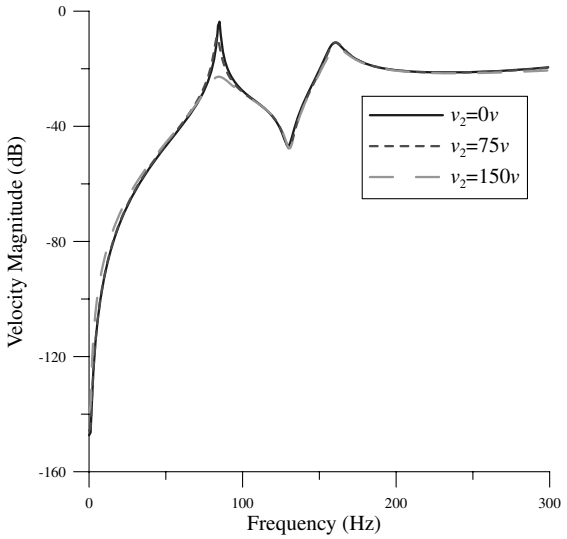

Fig. 12 Frequency response with $\bar{\tau} = 8$ N and $x_3 = 12.2$ cm.

For example, if the AMFC bimorph is moved to the left, its influence grows. Figure 12 displays the frequency response of the FEM if the AMFC bimorph is moved 3 cm to the left (i.e., $x_3 = 12.2$ cm). The nominal tension $\bar{\tau}$ is set to 8 N, and three voltage values for V_2 are tested. The shift in the natural frequency is more visible in this case.

IV. Conclusions

This paper explores a new approach for adaptive optics of membrane mirrors. It is proposed to augment membrane mirrors with smart actuators that can control their tension and shape. These actuators can be used to advantageously change the structural properties of membrane mirrors. It is demonstrated in the literature that structural characteristics of a circular lens could be used advantageously as an adaptive-optic deformable mirror for eliminating 100% of a fifth-order image aberration. To simplify the problem, the one-dimensional element of a membrane mirror is considered: a membrane strip. The membrane strip is modeled as an Euler–Bernoulli beam under tension. The FEM is used to obtain a state-space presentation of the system. The modeling process accounts for the added mass and stiffness of the bimorphs.

The membrane strip is augmented with two MFC bimorphs near its boundaries. The paper treats two configurations. For configuration 1, both bimorphs act in bending, whereas for configuration 2 one bimorph acts in bending and the other bimorph acts in tension. The model resulting from configuration 1 is a linear model that possesses two inputs. On the other hand, configuration 2 yields a nonlinear model. The nonlinearity is caused by the tension bimorph. Consequently, the tension bimorph is supplied with a constant voltage. The structure is then excited through the bending bimorph only.

Both models derived in this work assume perfect bonding between the MFC patches and the membrane strip. To fulfill this assumption, vacuum bagging is used to bond the membrane strip and the MFC patches. An experimental setup is used to verify the models derived. The results assert that the nominal tension exhibits a stiffening effect. For the cases surveyed, it was noticed that the voltage supplied to the tension bimorph has a softening effect. The error did not exceed 2% for all of the tests conducted. The work presented here can be potentially extended to the two-dimensional case.

Acknowledgments

Funding for this work is administered by the Center of Intelligent Material Systems and Structures (CIMSS) on behalf of the U.S. Air Force Office of Scientific Research under grant FA9550-06-1-0143. Special acknowledgment goes to Dan K. Marker of the U.S. Air Force Research Lab for motivating this work. The authors also acknowledge the fruitful and valuable discussions with Gyuhae Park of the Los Alamos National Laboratory Engineering Sciences and Application Division Office.

References

[1] Jenkins, C. (ed.), *Gossamer Spacecraft: Membrane and Inflatable Structures Technology for Space Applications*, Progress in Astonautics and Aeronautics, Vol. 191, AIAA, Reston, VA, 2001.

[2] Cassapakis, C., and Thomas, M., "Inflatable Structures Technology Development Overview," AIAA Space Programs and Technologies Conference, Huntsville, AL, AIAA Paper 1995-3738, Sept. 1995.

[3] Jenkins, C. (ed.), *Recent Advances in Gossamer Spacecraft*, Progress in Astronautics and Aeronautics, Vol. 212, AIAA, Reston, VA, 2006.

[4] Gorinevsky, D., and Hyde, T., "Adaptive Membrane for Large Lightweight Space Telescopes," *Highly Innovative Space Telescope Concepts*, Proceedings of the SPIE, Vol. 4849, SPIE–The International Society for Optical Engineering, Bellingham, WA, Dec. 2002, pp. 330–338.

[5] Davis, D., and Agnes, G., "Environmental Disturbance Modeling for Inflatable Space Structures," 43rd AIAA/ASME/ASCE/AHS Structures, Structural Dynamics, and Materials Conference, Denver, CO, AIAA Paper 2002-1266, Apr. 2002.

[6] Rogers, J., and Agnes, G. S., "Active Axisymmetric Optical Membranes," 43rd AIAA/ASME/ASCE/AHS Structures, Structural Dynamics, and Materials Conference, Denver, CO, AIAA Paper 2002-1450, Apr. 2002.

[7] Rogers, J., and Agnes, G. S., "Modeling Discontinuous Axisymmetric Active Optical Membranes," *Journal of Spacecraft and Rockets*, Vol. 40, No. 4, July–Aug. 2003.

[8] Sobers, D., Agnes, G., and Mollenhauer, D., "Smart Structures for Control of Optical Surfaces," 44th AIAA/ASME/ASCE/AHS/ASC Structures, Structural Dynamics, and Material Conference, Norfolk, VA, AIAA Paper 2003-1559, Apr. 2003.

[9] Ruggiero, E., Jha, A., Park, G., and Inman, D., "A Literature Review of Ultra-Light and Inflated Toroidal Satellite Components," *The Shock and Vibration Digest*, Vol. 35, No. 3, May 2003, pp. 171–181.

[10] Ruggiero, E., Jacobs, J., and Babb, B., "A SPIDER Technology Overview," 45h AIAA/ASME/ASCE/AHS/ASC Structures, Structural Dynamics and Material Conference, Palm Springs, CA, AIAA Paper 2004-1822, Apr. 2004.

[11] Wong, Y., and Pelligrino, S., "Computation of Wrinkle Amplitude in Thin Membranes," 43rd AIAA/ASME/ASCE/AHS/ASC Structures, Structural Dynamics and Material Conference, Denver, CO, AIAA Paper 2002-1369, Apr. 2002.

[12] Wong, Y., and Pelligrino, S., "Prediction of Wrinkle Amplitudes in Square Solar Sails," 44th AIAA/ASME/ASCE/AHS/ASC Structures, Structural Dynamics and Material Conference, Norfolk, VA, AIAA Paper 2003-1982, Apr. 2003.

[13] Ruggiero, E., and Inman, D., "Gossamer Spacecraft: Recent Trends in Design, Analysis, Experimentation and Control," *Journal of Spacecraft and Rockets*, Vol. 43, No. 1, Jan. 2006, pp. 10–24.

[14] Shepherd, M., Peterson, G., Cobb, R., and Palazotto, A., "Quasi-Static Optical Control of In-Plane Actuated, Deformable Mirror: Experimental Comparison with Finite Element Analysis," 47th AIAA/ASME/ASCE/AHS/ASC Structures, Structural Dynamics, and Material Conference, Newport, RI, AIAA Paper 2006-2231, May 2006.

[15] Peng, F., Hu, Y.-R., and Ng, A., "Testing of Membrane Space Structure Shape Control Using Genetic Algorithm," *Journal of Spacecraft and Rockets*, Vol. 43, No. 4, 2006, pp. 788–793.

[16] Marker, D., and Jenkins, C., "Surface Precision of Optical Membranes with Curvature," *Optics Express*, Vol. 1, No. 11, 1997, pp. 324–331.

[17] Marker, D., Rotge, J., Carreras, R., Duneman, D., and Wilkes, J., "Minimum Strain Requirements for Optical Membranes," *High-Resolution Wavefront Control: Methods, Devices and Applications*, Proceedings of the SPIE, Vol. 3760, SPIE–The International Society for Optical Engineering, Bellingham, WA, Nov. 1999, pp. 224–231.

[18] Wilkes, J., Jenkins, C., Marker, D., Carreras, R., Duneman, D., and Rotge, J., "Concave Membrane Mirrors from Aspheric to Near Parabolic," *High-Resolution Wavefront Control: Methods, Devices and Applications*, Proceedings of the SPIE, Vol. 3760, SPIE–The International Society for Optical Engineering, Bellingham, WA, Nov. 1999, pp. 213–223.

[19] Vdovin, G., Sarro, P., Gonté, F., Collings, N., and Dandliker, R., "Recent Progress in Technology and Applications of Membrane Micromachined Deformable Mirrors," *High-Resolution Wavefront Control: Methods, Devices and Applications*, Proceedings of the SPIE, Vol. 3760,SPIE–The International Society for Optical Engineering,

Bellingham, WA, Nov. 1999, pp. 2–11.
[20] Pollard, E., deBlonk, B., Erwin, R., and Jenkins, C., "Characterizing the Non-Linear Behavior of Membrane Optics," *Space Systems Engineering and Optical Alignment Mechanisms*, Proceedings of the SPIE, Vol. 5528, SPIE–The International Society for Optical Engineering, Bellingham, WA, Oct. 2004, pp. 181–191.
[21] Ruggiero, E., "Modeling and Control of SPIDER Satellite Components," Ph.D. Dissertation, Department of Mechanical Engineering, Virginia Polytechnic Inst. and State Univ., Blacksburg, VA, July 2005.
[22] Moore, J., Patrick, B., Chodimella, S., Marker, D., and deBlonk, B., "Design and Testing of a One-Meter Membrane Mirror with Active Boundary Control," *UV/Optical/IR Space Telescopes: Innovative Technologies and Concepts 2*, Proceedings of the SPIE, Vol. 5899, SPIE–The International Society for Optical Engineering, Bellingham, WA, Aug. 2005, pp. 340–346.
[23] Chodimella, S., Moore, J., and Patrick, B., "Design, Fabrication, and Validation of an Ultra-Lightweight Membrane Mirror," *Advanced Wavefront Control: Methods, Devices, and Applications 3*, Proceedings of the SPIE, Vol. 5894, SPIE–The International Society for Optical Engineering, Bellingham, WA, Aug. 2005, pp. 351–359.
[24] Patrick, B., Moore, J., Chodimella, S., Marker, D., and deBlonk, B., "Final Testing and Evaluation of a Meter-Class Actively Controlled Membrane Mirror," 47th AIAA/ASME/ASCE/AHS/ASC Structures, Structural Dynamics, and Material Conference, Newport, RI, AIAA Paper 2006-1901, May 2006..
[25] Korde, U., Jenkins, C., Farke, J., and Hofacker, M., "Adaptive Rectangular Membranes Actuated Near Boundaries," *Smart Structures and Materials 2006: Smart Structures and Integrated Systems*, Proceedings of the SPIE, Vol. 6173, SPIE–The International Society for Optical Engineering, Bellingham, WA, Apr. 2006, pp. 263–271.
[26] Hall, J., Glaese, R., and Flint, E., "Dynamic Behavior of Thin Film Membrane Strips," 43rd AIAA/ASME/ASCE/AHS Structures, Structural Dynamics, and Materials Conference, Denver, CO, AIAA Paper 2002-1378, Apr. 2002.
[27] Renno, J., Tarazaga, P., Seigler, M., and Inman, D., "Modeling of a Membrane Mirror Actuated Using Piezoelectric Bimorph," 2006 ASME International Mechanical Engineering Congress and Exposition (IMECE2006), Chicago, IL, American Society of Mechanical Engineers, Paper IMECE2006-13224, Nov. 2006.
[28] Renno, J., and Inman, D., "Modeling of a Membrane Mirror Strip Actuated Using Multiple Active Fiber Composites," Conference & Exposition on Structural Dynamics (IMAC-25), Orlando, FL, Society for Experimental Mechanics, Paper IMAC-204, Feb. 2007.
[29] Wilkie, W., Bryant, R., High, J., Fox, R., Hellbaum, R., Jalink, A., Little, B., and Mirick, P., "Low-Cost Piezocomposite Actuator for Structural Control Application," *Smart Structures and Materials 2000*, Proceedings of the SPIE, Vol. 3987, SPIE–The International Society for Optical Engineering, Bellingham, WA, 2000, pp. 323–334.
[30] Malacara, D., *Optical Shop Testing, Pure and Applied Optics*, 2nd ed., Wiley, New York, 1992.
[31] Tyson, R. K., *Introduction to Adaptive Optics*, SPIE Tutorial Texts in Optical Engineering, Vol. TT41, SPIE Press, Bellingham, WA, Mar. 2000.
[32] Inman, D., *Engineering Vibrations*, Prentice–Hall, Upper Saddle River, NJ, 2000.
[33] Banks, H., Wang, Y., Inman, D., and Slater, J., "Approximation and Parameter Identification for Damped Second Order Systems with Unbounded Input Operators," *Control Theory and Advanced Technology*, Vol. 10, 1994, pp. 873–892.
[34] Banks, H., Smith, R., and Wang, Y., *Smart Material Structures: Modeling, Estimation and Control*, Wiley, Toronto, 1996.
[35] Banks, H., Inman, D., Leo, D., and Wang, Y., "An Experimentally Validated Damage Detection Theory in Smart Structures," *Journal of Sound and Vibration*, Vol. 191, No. 5, 1996, pp. 859–880.
[36] Strang, G., and Fix, G., *An Analysis of the Finite Element Method*, Prentice–Hall, Upper Saddle River, NJ, 1973.
[37] Prenter, P., *Splines and Variational Methods*, Wiley, New York, 1975.
[38] DeBoor, C., Hollig, K., and Riemenschneider, S., *Box Splines*, Applied Mathematical Sciences, Vol. 98, Springer–Verlag, New York, 1992.
[39] Hollig, K., *Finite Element Methods with B-Splines*, Frontiers in Applied Mathematics, Society of Industrial and Applied Mathematics, Philadelphia, 2001.

L. Peterson
Associate Editor